Journal of
Applied Crystallography
ISSN 0021-8898

Received 16 August 2006
Accepted 13 November 2006

Structure of nanoporous zirconia-based powders synthesized by different gel-combustion routes

Jorge R. Casanova,[a] Ismael O. Fábregas,[a] Diego G. Lamas,[a] Noemí E. Walsöe de Reca,[a] Gustavo E. Lascalea,[b] Rodolfo Kempf,[c] Aldo F. Craievich[d]* and Celso V. Santilli[e]

[a]CINSO, CITEFA-CONICET, J. B. de La Salle 4397, (1603) Villa Martelli, Pcia. de Buenos Aires, Argentina, [b] CRICYT, CONICET, Av. Ruíz Leal s/n - Parque General San Martín - C.C. 131, (5500) Mendoza, Pcia. de Mendoza, Argentina, [c]UACN, Centro Atómico Constituyentes, CNEA, (1650) San Martín, Pcia. de Buenos Aires, Argentina, [d]Instituto de Física, Universidade de São Paulo, Cidade Universitária, (05508-900) São Paulo, SP, Brazil, and [e]Instituto de Química /UNESP, Departamento de Físico-Química, PO Box 355, (14801-970) Araraquara, SP, Brazil. Correspondence e-mail: craievich@if.usp.br

Zirconia-based ceramics that retain their metastable tetragonal phase at room temperature are widely studied due to their excellent mechanical and electrical properties. When these materials are prepared from precursor nanopowders with high specific surface areas, this phase is retained in dense ceramic bodies. In this work, we present a morphological study of nanocrystalline ZrO_2–2.8 mol% Y_2O_3 powders synthesized by the gel-combustion method, using different organic fuels – alanine, glycine, lysine and citric acid – and calcined at temperatures ranging from 873 to 1173 K. The nanopore structures were investigated by small-angle X-ray scattering. The experimental results indicate that nanopores in samples prepared with alanine, glycine and lysine have an essentially single-mode volume distribution for calcination temperatures up to 1073 K, while those calcined at 1173 K exhibit a more complex and wider volume distribution. The volume-weighted average of the nanopore radii monotonically increases with increasing calcination temperature. The samples prepared with citric acid exhibit a size distribution much wider than the others. The Brunauer–Emmett–Teller technique was used to determine specific surface area and X-ray diffraction, environmental scanning electron microscopy and transmission electron microscopy were also employed for a complete characterization of the samples.

1. Introduction

Zirconia-based ceramics have been intensely investigated because of their excellent electric and mechanical properties. In particular, TZP ('tetragonal zirconia polycrystals') ceramics exhibit high ionic conductivity at intermediate temperatures and high fracture toughness (Lee & Rainforth, 1994; Juárez *et al.*, 1999).

Pure zirconia exhibits three stable phases over different temperature ranges with monoclinic, tetragonal and cubic structures (Lee & Rainforth, 1994; Juárez *et al.*, 1999). The monoclinic phase is stable below 1473 K, the tetragonal phase between 1473 and 2553 K, and the cubic phase above 2553 K. The cubic phase can be fully stabilized at room temperature in solid solutions with other oxides such as Y_2O_3, CaO, MgO, CeO_2 *etc.* In contrast, even if dopant oxides are added, the tetragonal phase can only be retained in a metastable condition in nanocrystalline powders or fine-grained ceramics (Juárez *et al.*, 1999).

The zirconia-based materials mentioned above have many applications. For example, ZrO_2–CeO_2 substitutional solid solutions are extensively used as redox or oxygen storage promoters in three-way catalysts (Trovarelli, 2002) and ZrO_2–Y_2O_3 ceramics are used for several electrochemical devices (Déportes *et al.*, 1994) and biomedical applications (Yaparpalvi *et al.*, 1994).

In previous investigations, different routes for the synthesis of nanocrystalline ZrO_2–2.8 mol% Y_2O_3 powders by the gel-combustion method were developed. Several organic fuels – such as citric acid or the amino acid glycine – were employed (Juárez *et al.*, 2000; Lascalea *et al.*, 2004). The gel-combustion method is based on the formation of an initial gel by thermal concentration of an aqueous solution of nitrates of the desired cations, followed by a combustion process. The reaction between nitrate ions and the organic fuel is strongly exothermic. The large volume of gases produced during the combustion reaction promotes the disintegration of the precursor gel. This process is followed by calcination, which eliminates the organic residuals and yields small grains containing crystals of nanometre sizes. The rapid combustion reaction also promotes the formation of very small pores inside the grains that are not fully eliminated during the calcination process.

The morphology of the final nanopowders on the nanometre scale depends on (i) the size of the basic nanocrystals, (ii) the sizes of the grains and (iii) the concentration and features of the intra-grain nanoporosity. In this work, we have characterized the nanoporosity of ZrO_2–2.8 mol% Y_2O_3 powders synthesized using different organic fuels – citric acid, alanine, glycine and lysine – by small-angle X-ray scattering (SAXS). Other techniques, such as X-ray diffraction

(XRD), Brunauer-Emmett-Teller (BET) specific surface area measurements, environmental scanning electron microscopy (ESEM) and transmission electron microscopy (TEM), were also employed for the characterization of the nanopowders.

2. Materials and characterization techniques

2.1. Samples

ZrO_2–2.8 mol% Y_2O_3 nanopowders were synthesized by the gel-combustion method starting from $ZrOCl_2{\cdot}8H_2O$ and Y_2O_3. These reagents were dissolved in a controlled excess of HNO_3. This nitrate solution was then concentrated on a hot plate until the complete removal of chlorine. The chosen fuel (citric acid, alanine, glycine or lysine) was added and the pH of the solution was adjusted with NH_4OH to as close to pH = 7 as possible, but trying to avoid any noticeable precipitation. In practice, the desired value pH = 7 was only reached without any precipitation in the case of the citric acid route, while the maximum possible pH was about 4 for the other fuels. The resulting solution was then concentrated on a hot plate at 473 K until a viscous gel was obtained, which finally burned due to a vigorous exothermic reaction. Stainless steel vessels were used for all the syntheses.

The fuel proportions are usually expressed in relation to the cation concentration of the precursor solution to be processed. In order to standardize the reducting power in these syntheses for comparison purposes, we have applied the criterion of balancing the product between the mole number of the fuel and its 'oxidizing valence'. This means that two synthetic processes are considered equivalent if $n(\mathrm{C1})V(\mathrm{C1}) = n(\mathrm{C2})V(\mathrm{C2})$, where $n(\mathrm{C}i)$ and $V(\mathrm{C}i)$ are the mole number and the oxidizing valence of fuel i, respectively. The oxidizing valence is a parameter used in propellant and explosive calculations, and is evaluated using a formula proposed by Jain *et al.* (1981). In these calculations, it is assumed that the oxidizing valences of the elements present in the fuels are $V(\mathrm{O}) = -2$; $V(\mathrm{N}) = 0$; $V(\mathrm{C}) = 4$ and $V(\mathrm{H}) = 1$. Then, the oxidizing valence of a generic compound $C_nH_mO_sN_t$ is calculated as: $V(C_nH_mO_sN_t) = 4n + m - 2s$. In recent work (Lascalea *et al.*, 2004), the amount of glycine that is needed in order to obtain the highest specific surface area in the final material was optimized. The optimum amount of glycine was of 5 moles per mole of metal cations. Using the proposed equivalence criterion, the following optimum amounts were established for the other fuels: 2.5 moles citric acid, 3 moles alanine and 1.3 moles lysine, all of them per mole of metal cations. These fuel/metal proportions were employed in this work.

For removal of volatile residuals, the resulting white ashes from the ZrO_2–Y_2O_3 samples prepared with citric acid, alanine, glycine or lysine as fuels were calcined in air for 2 h at different temperatures ranging from 873 to 1173 K. It is worth mentioning that the powders treated within this temperature range consist in all cases of very small nanocrystals. In powders treated at higher temperatures, a coarser crystalline structure develops.

2.2. XRD, ESEM, TEM and BET techniques

The crystal structure of the zirconia-based powders was studied by XRD using a Philips PW3710 powder diffractometer with Cu $K\alpha$ radiation. The average crystallite sizes were determined from the width of the (111) peak (after subtraction of the contribution to peak broadening due to instrumental effects) by means of the Scherrer equation.

Morphological studies were carried out by ESEM (Philips Electroscan 2010) and TEM (Philips CM200). The specific surface areas of the powders were measured by the BET technique using Quantachrome Autosorb-1-C equipment.

2.3. SAXS setup

SAXS measurements were performed using the synchrotron D11A-SAXS1 beamline of LNLS, Campinas, Brazil. This beamline is equipped with an asymmetrically cut and horizontally bent Si(111) monochromator that provides a horizontally focused X-ray beam with a wavelength $\lambda = 1.608$ Å. The SAXS intensity was recorded along the vertical direction using a Biologic one-dimensional position-sensitive X-ray gas detector as a function of the modulus of the scattering vector q, defined as $q = (4\pi/\lambda)\sin(\varepsilon/2)$, ε being the scattering angle. The samples characterized by SAXS in transmission mode were ZrO_2-based powders placed between two thin mica discs.

Two SAXS patterns were collected for each sample using detector slits of 0.5 and 8 mm, respectively. The use of a 0.5 mm slit is better for minimizing smearing effects on the measured scattering intensity at very small q. However, using this narrow slit, the counting rate at high q is too weak. Therefore, in order to enhance the counting rate while keeping negligible smearing effects over the high q range, we also measured the SAXS intensity produced by the same samples using a wider (8 mm) slit. The parasitic scattering from the slits and mica windows were then subtracted and the resulting curves were normalized to equivalent intensity of the direct X-ray beam and same sample thickness. Finally, both of the patterns collected with 0.5 and 8 mm detector slits were properly merged.

2.4. SAXS analysis

The system studied here is modelled as a dense material matrix in which a polydisperse set of nanopores is embedded. The nanoporosity that is inside ZrO_2-based grains is assumed to be the dominant source of SAXS. In order to analyse the experimental data, we have applied a simple two-electron-density model consisting of an isotropic, dilute and polydisperse set of spherical nanopores (with an electron density $\rho_1 \simeq 0$) embedded in a homogeneous matrix with density ρ_0. For this model, the SAXS intensity is given by

$$I(q) = \int_0^\infty N(R) I_1(q, R)\, \mathrm{d}R, \tag{1}$$

where $N(R)$ is the number of nanopores per unit radius R and $I_1(q, R)$ is the SAXS intensity produced by a single spherical object of radius R,

$$I_1(q, R) = (\Delta\rho)^2 \left(\frac{4}{3}\pi R^3\right)^2 \left[\frac{3(\sin qR - qR\cos qR)}{(qR)^3}\right]^2, \tag{2}$$

where $\Delta\rho$ is the difference in electron density between the two phases. In the case of pore 'particles' embedded in a homogenous matrix, $\Delta\rho$ is assumed to be equal to ρ_0.

The integral equation (1) was solved using the *GNOM* software (Svergun, 1992), the input to which is the experimental SAXS intensity curves corresponding to the studied materials after subtraction of the parasitic scattering intensity and the output is the nanopore volume distribution function

$$V(R) = (4/3)\pi R^3 N(R). \tag{3}$$

The SAXS intensity function for a porous structure that can be modelled as a two-electron-density system consisting of a dilute and isotropic set of nano-objects or particles exhibits two asymptotic behaviours at low and at high q, defined by the Guinier and Porod equations, respectively. The Guinier equation (Guinier & Fournet, 1955) allows one to determine an average value of the radius of

Table 1
Average crystallite size (D) and BET specific surface area (A) for samples calcined at 873 K.

Fuel	D (Å)	A ($m^2\ g^{-1}$)
Lysine	130 ± 10	15.8 ± 0.3
Glycine	130 ± 10	14.2 ± 0.3
Alanine	110 ± 10	16.3 ± 0.4
Citric acid	140 ± 10	13.6 ± 0.3

gyration that weights large particles much more than small ones. This equation is in practice only useful for systems of particles with not too wide a size distribution. In the high-q limit, the SAXS intensity by two-electron-density systems (particulate or not) with a sharp interface obeys the Porod equation (Porod, 1982),

$$I(q) = 2\pi(\Delta\rho)^2(S/q^4), \tag{4}$$

which in our case can be applied to determine the interface surface area, S, between the solid material and the nanopores. The Porod equation holds for isotropic two-electron-density systems with sharp interfaces, including those composed of particles (or pores) of any shape except very narrow needle-like or thin disc-like nano-objects. In the particular case of a dilute set of spherical particles, the total surface area can alternatively be determined from the *GNOM* output function $V(R)$ as

$$S = \int_0^\infty 4\pi R^2 N(R)\,\mathrm{d}R = 3\int_0^\infty [V(R)/R]\,\mathrm{d}R. \tag{5}$$

Equations (1), (4) and (5) were applied to characterize the nanopore structure of all ZrO_2-based materials studied here. Nevertheless, since our SAXS measurements were not performed in absolute units, the data analysis only yields $N(R)$, $V(R)$ and S on a relative scale. Even though several results reported here are quantities proportional to $N(R)$, $V(R)$ and S, these parameters, on a relative scale, are useful for comparison purposes when they refer, for example, to the nanoporosity developed in various samples prepared with different fuels and to changes due to differences in calcination temperatures.

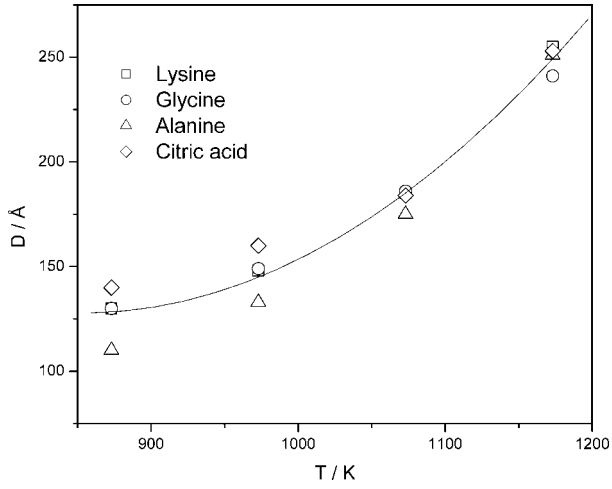

Figure 1
Average crystallite size, D, corresponding to samples prepared with different fuels as a function of the calcination temperature.

3. Results

3.1. XRD, BET, ESEM and TEM studies

Our XRD study indicated that the high temperature tetragonal phase was fully retained at room temperature in all the samples studied. No Bragg reflections corresponding to the monoclinic phase were detected.

The average crystallite sizes of all the samples studied were determined from the width of the (111) peak by means of the Scherrer equation after subtraction of the instrumental broadening, evaluated using an α-Al_2O_3 standard powder. The average crystallite sizes, D, determined from the width of the Bragg peak profiles for samples calcined at 873 K, are reported in Table 1. These average sizes range from 110 to 140 Å for samples prepared with different fuels. Fig. 1 exhibits the average crystallite size as a function of calcination temperature for all the gel-combustion routes used in this work. The average crystallite size increases monotonically with increasing calcination temperature.

BET specific surface areas, A, for powders prepared using different organic fuels and calcined at 873 K are listed in Table 1. We can notice that different combustion routes lead to similar surface areas, the maximum value corresponding to the powder synthesized using alanine as fuel.

An ESEM study indicated that powders prepared with different fuels exhibit similar morphology on the microscopic scale. They are composed of porous agglomerates with sizes ranging from 50 to 100 µm. Bright-field TEM observations such as that shown in Fig. 2 suggested that, on a finer scale, these large agglomerates are composed of small aggregates of nanoparticles. Since a clear correlation between the shapes and sizes derived from bright-field and dark-field images was noticed, it was inferred that the nanoparticles observed in the bright-field images are, in fact, nanoscopic crystallites. The average sizes of these nanoparticles are similar to the average crystallite sizes derived from XRD patterns. We can remark in Fig. 2 that the large pores are readily visible but the details of the nano-

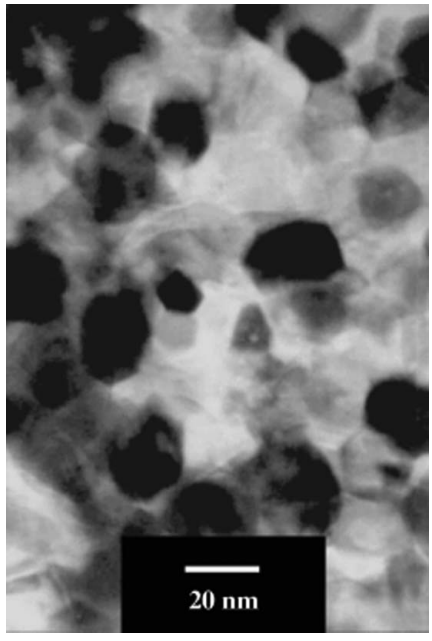

Figure 2
Bright-field TEM image displaying a typical morphology of a final powder synthesized using citric acid as fuel and calcined at 873 K.

porosity developed inside the grains and characterized by SAXS are not clearly apparent. For this reason, we have not performed a systematic and quantitative TEM study for the characterization of the variations in nanoporosity for different fuels and as a function of the calcination temperature.

3.2. SAXS study

SAXS patterns of all ZrO_2–2.8 mol% Y_2O_3 powders studied here are displayed in Fig. 3 on a log–log scale. All SAXS curves follow an asymptotic linear behaviour at high q, with a slope approximately equal to −4, thus indicating that the SAXS intensity obeys in all cases the Porod equation [equation (4)]. Therefore, this finding supports the two-electron-density model that is proposed here in order to describe the porous structure on the nanometre scale.

It should be pointed out that nanoporous structures are expected to be developed in xerogels subjected to medium and high temperature treatments, at which organic species evaporate partially or totally from the bulk. This nanoporosity has been quantitatively characterized for many xerogels, such as those based on SnO_2 (Santilli *et al.*, 1995) and SiO_2 (Colomer & Anderson, 2001). We did not find any experimental evidence in the present work about a possible alternative source for the observed SAXS such as, for example, atomic nanophase separation. In fact, the presence of atomic nanophase separation would produce a very weak SAXS intensity because the atomic numbers of Zr and Y are similar and, consequently, the contrast in electron density would be very small.

The SAXS curves plotted in Fig. 3 corresponding to samples synthesized with alanine, glycine or lysine and calcined at 873 K exhibit a 'knee' at q-values close to 0.07 Å^{-1}. This feature shifts towards lower q values with increasing calcination temperature. In order to analyse our SAXS data we have assumed that the X-ray scattering intensity is due to isolated and spatially uncorrelated nanopores embedded in an essentially homogeneous matrix. Under this assumption, the knees observed in the SAXS curves plotted in Fig. 3 indicate a preferred nanopore size with a rather wide size distribution. This feature is not apparent in the SAXS curves corresponding to samples prepared with citric acid as fuel.

The volume distribution functions of nanopore radii $V(R)$ corresponding to powders prepared with alanine, glycine and lysine as fuels were determined using the *GNOM* program (Fig. 4). For these samples, the modelled $I(q)$ functions corresponding to the best fit to the experimental SAXS data are shown in Fig. 3 (solid lines). In contrast, no satisfactory *GNOM* outputs were obtained for the SAXS curves corresponding to powders prepared with citric acid as fuel and calcined at different temperatures. In these cases a nearly linear dependence of the SAXS intensity on a log–log scale over most of the q range is observed, thus suggesting a very wide pore volume distribution without a preferred pore size.

The pores between the powder grains are much larger than the nanopores inside the grains. Thus, we expect that the contribution to the SAXS intensity from the comparatively large pores would be concentrated within a range of very low q values. In this respect, we remark in Fig. 3 that positive deviations of the SAXS intensity from the fitted curves are apparent at very small q values in several experimental SAXS spectra. The fitted part of the SAXS curves corresponding to alanine, glycine and lysine are related to the

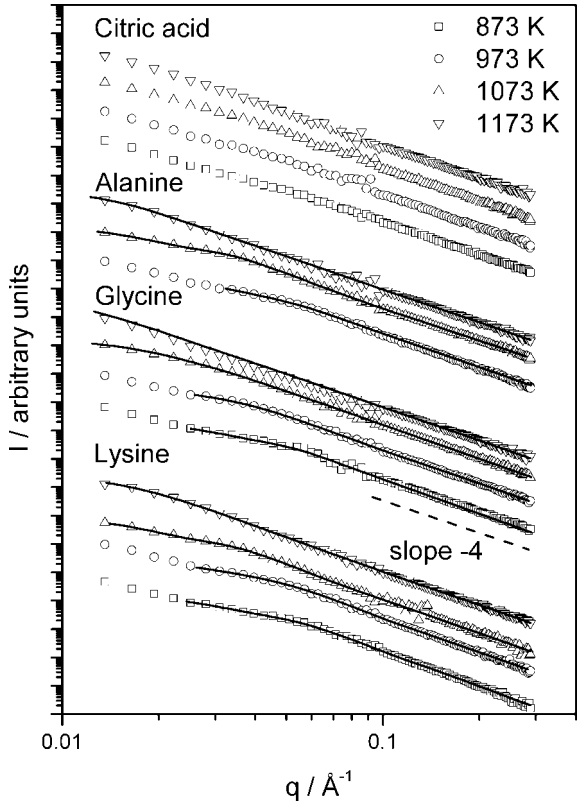

Figure 3
SAXS intensity curves on a log–log scale for all the samples studied in this work. The best fits of the modelled SAXS functions derived by the *GNOM* program for samples synthesized with alanine, glycine or lysine as fuel are shown as solid lines. The patterns are vertically shifted for clarity.

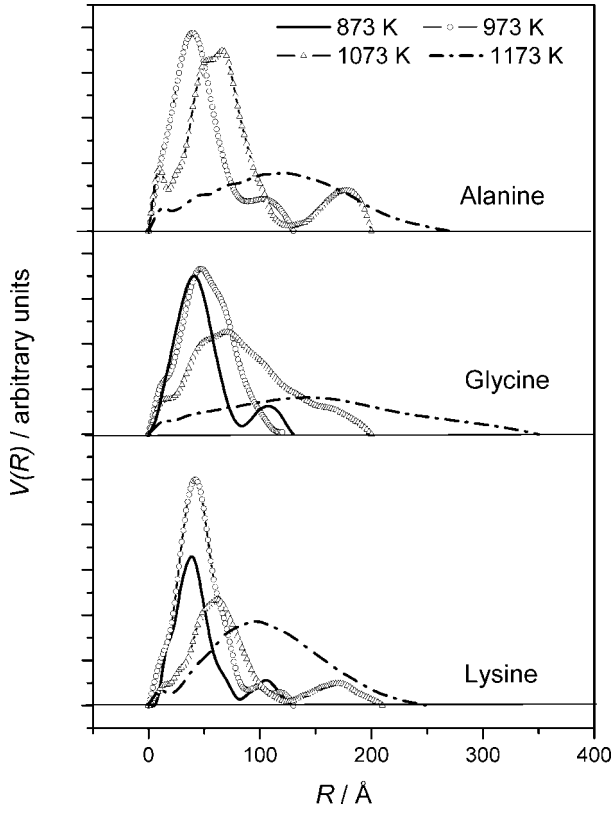

Figure 4
Volume distribution function $V(R)$ obtained from SAXS data using the *GNOM* software for samples synthesized with alanine, glycine or lysine as fuels.

nanometre-sized pores inside the powder grains. Most of the additional contribution to the SAXS intensity produced by the rather large inter-grain pores could not be detected by our SAXS setup for which $q_{min} = 0.012$ Å^{-1}.

4. Discussion

The nanopore radius corresponding to the maximum of the volume distribution, $R(V_{max})$, is plotted in Fig. 5(*a*) as a function of the calcination temperature for different gel-combustion routes. $R(V_{max})$ was considered as an approximate estimate for the volume-weighted average of pore radii. This value remains approximately constant for calcination temperatures between 873 and 973 K and increases for $T > 973$ K. On the other hand, the half-maximum width of the main mode of the $V(R)$ functions, W, plotted in Fig. 5(*b*), exhibits a similar increasing trend with the calcination temperature, as expected according to the classic theory of Ostwald ripening developed by Lifshitz & Slyozov (1961). These features indicate that calcination at increasing temperatures leads to a progressively coarser nanoporosity.

It is worth noticing that the average crystallite size D and the nanopore radius $R(V_{max})$ plotted in Figs. 1 and 5(*a*), respectively, exhibit similar increasing trends as functions of the calcination temperature. This feature indicates that the processes for nanocrystal and for nanopore growths at different temperatures are closely correlated. The results plotted in Fig. 6 corresponding to samples prepared with alanine, glycine or lysine as fuels and calcined at different temperatures indicate a roughly linear relation between $R(V_{max})$ and D. This finding suggests that the nanopores are located between the nanometre-sized crystallites that build up the larger micrometre-sized grains. Under this hypothesis, it is expected that the growth of the nanocrystallites induces a correlated increase in nanopore sizes. On the other hand, the nanoporosity is also affected by its own coarsening process, *i.e.* the larger nanopores growing at the expense of the small ones, this parallel and classical effect being expected to occur simultaneously with the process of crystallite growth.

Fig. 7 exhibits the nanopore surface area, S_T, in relative units, as a function of the calcination temperature for different samples. The surface area was determined by using the Porod equation [equation (4)] for all the samples studied and by equation (5) only for powders synthesized with alanine, glycine and lysine. Both procedures yielded similar results. We can notice that the nanopore surface area and its dependence on the calcination temperature are similar for all gel-combustion routes. In addition, S_T increases for calcination

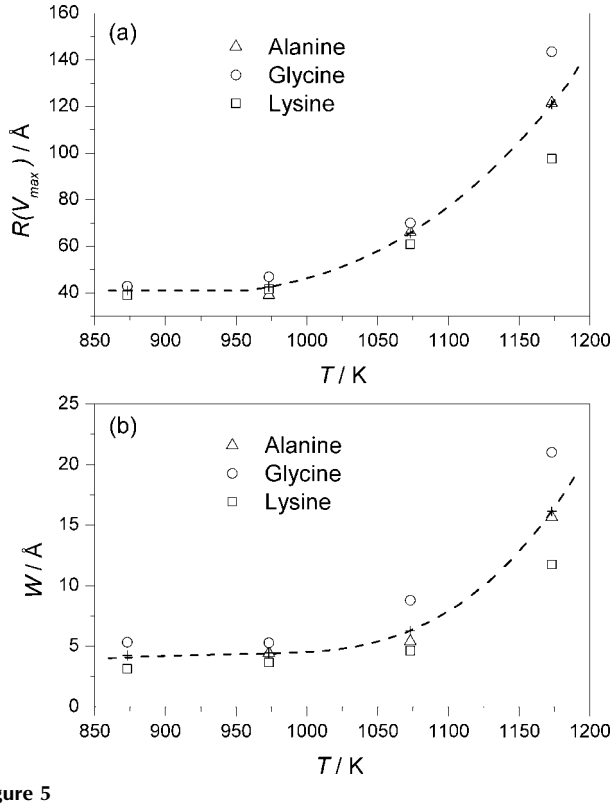

Figure 5
(*a*) Nanopore radius corresponding to the maximum of the volume distribution, $R(V_{max})$ and (*b*) half-maximum width of the main mode of $V(R)$, W, as functions of calcination temperature for samples synthesized with alanine, glycine or lysine as fuel.

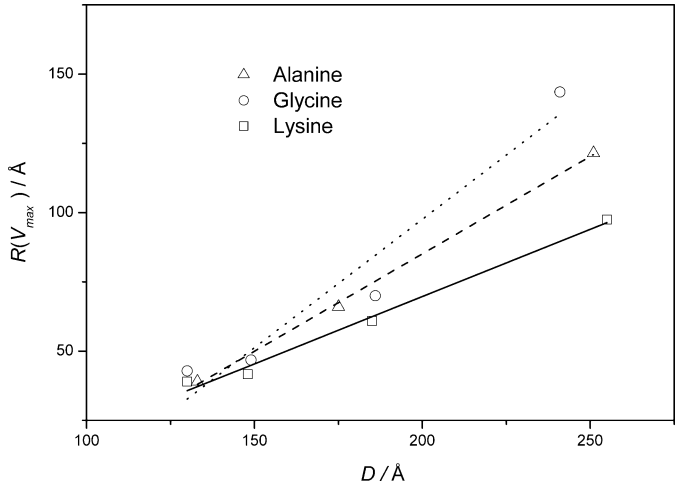

Figure 6
Nanopore radius corresponding to the maximum of the volume distribution, $R(V_{max})$, as a function of crystallite size, D, for samples prepared with alanine, glycine or lysine as fuel, calcined at different temperatures. The straight lines are guides for the eyes.

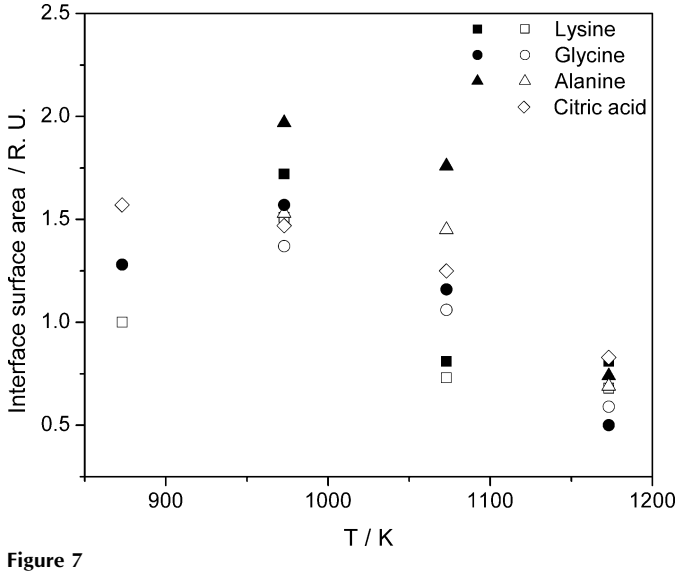

Figure 7
Interface surface area (in relative units, assuming a value of unity for the sample synthesized with lysine as fuel and calcined at 873 K) determined by using equation (4) (empty symbols) and equation (5) (filled symbols).

temperatures between 873 and 973 K and decreases for temperatures higher than 973 K. The increasing trend of S_T is probably due to variations in surface area induced by evaporation of remaining volatile species. The decrease observed for higher calcination temperatures is the expected classical effect for a dominant process of nanopore coarsening.

5. Conclusions

ZrO_2–2.8 mol% Y_2O_3 nanopowders synthesized by the gel-combustion route using alanine, glycine, lysine and citric acid as fuels are composed of grains with crystallite sizes ranging from 110 to 255 Å for calcination temperatures rising from 873 to 1173 K. The tetragonal phase is fully retained at room temperature in all the powders studied.

The SAXS results presented here indicate that the morphology of nanostructured ZrO_2-based materials synthesized by the gel-combustion route can be modelled as a two-electron-density system. Powders prepared with alanine, glycine and lysine as fuels exhibit a fine porous structure consisting of nearly spherical and isolated nanopores with a rather narrow volume weighted radius distribution centred at 30–45 Å for calcination temperatures ranging from 873 to 973 K and with a much larger size distribution for higher temperatures (1073–1173 K). Powders synthesized with citric acid exhibit a much wider pore radius distribution for all calcination temperatures. It is worth noticing that citric acid is not an amino acid, while the other three fuels are, thus the fact that citric acid leads to a different and much wider nanopore size distribution is probably connected to the nature of the organic structure of the fuel. The relationship between the nature of the structure of the organic fuel and the nanoporosity developed in the final powders will be investigated in future work.

The results presented here suggest that nanopores in ZrO_2-based powders prepared by the gel-combustion route are located between nanometre-sized crystallites that build up the powder grains. For increasing calcination temperature, both structural entities (nanocrystals and nanopores) are subjected to the same coarsening effect, *i.e.* the growth of the nanocrystallites, inducing a correlated increase in nanopore sizes. Finally, no significant effects of the nature of the fuel on the crystallite and nanopore morphologies were detected.

The authors thank LNLS, CAPES/SECyT, CNPq/CONICET, CLAF, CNPq (PROSUL program), ANPCyT and CONICET for proving funding. The help of E. D. Cabanillas (CAC, CNEA, Argentina) in the TEM study is also acknowledged.

References

Colomer, M. T. & Anderson, M. A. (2001). *J. Non-Cryst. Solids*, **290**, 93–104.
Déportes, C., Duclot, M., Fabry, P., Fouletier, J., Hammou, A., Kleitz, M., Siebert, E. & Souquet, J.-L. (1994). *Electrochimie des Solides*. Grenoble: Presses Universitaires de Grenoble. (In French.)
Guinier, A. & Fournet, G. (1955). *Small-Angle Scattering of X-rays*, ch. 2. New York: Wiley.
Jain, S. R., Adiga, K. C. & Verneker, V. R. (1981). *Combust. Flame*, **40**, 71–79.
Juárez, R. E., Lamas, D. G., Lascalea, G. E. & Walsöe de Reca, N. E. (1999). *Defect Diffus. Forum*, **177–78**, 1–26.
Juárez, R. E., Lamas, D. G., Lascalea, G. E. & Walsöe de Reca, N. E. (2000). *J. Eur. Ceram. Soc.* **20**, 133–138.
Lascalea, G. E., Lamas, D. G., Pérez, L., Cabanillas, E. D. & Walsöe de Reca, N. E. (2004). *Mater. Lett.* **58**, 2456–2460.
Lee, W. E. & Rainforth, W. M. (1994). *Ceramic Microstructures: Property Control by Processing*, p. 317. London: Chapman and Hall.
Lifshitz, I. M. & Slyozov, V. V. (1961). *J. Phys. Chem Solids*, **19**, 35–50.
Porod, G. (1982). *Small Angle X-ray Scattering*, edited by O. Kratky and O. Glatter, pp. 17–51. London: Academic Press.
Santilli, C. V., Pulcinelli, S. H. & Craievich A. F. (1995). *Phys. Rev. B*, **51**, 8801–8809.
Svergun, D. (1992). *J. Appl. Cryst.* **25**, 495–503.
Trovarelli, A. (2002). *Catalysis by Ceria and Related Materials*. London: Imperial College Press.
Yaparpalvi, R., Loyalka, S. K. & Tompson, R. V. J. Jr(1994). *Biomed. Mater. Res.* **28**, 1087–1093.